

# ADVANCED FUNCTIONAL MATERIALS

## Supporting Information

for *Adv. Funct. Mater.*, DOI: 10.1002/adfm.201702485

Near-Infrared and Short-Wavelength Infrared Photodiodes  
Based on Dye–Perovskite Composites

*Qianqian Lin, Zhiping Wang, Margaret Young, Jay B. Patel,  
Rebecca L. Milot, Laura Martinez Maestro, Richard R. Lunt,  
Henry J. Snaith, Michael B. Johnston, and Laura M. Herz\**

## Supporting Information

### **Near-infrared and short-wavelength infrared photodiodes based on dye-perovskite composites**

*Qianqian Lin, Zhiping Wang, Margaret Young, Jay B. Patel, Rebecca L. Milot, Laura M. Maestro, Richard R. Lunt, Henry J. Snaith, Michael B. Johnston, Laura M. Herz\**

1. Experimental section
2. Supporting figures

## Experimental Section

### *Preparation of perovskite and dye precursors:*

(1) Formamidinium iodide synthesis:  $\text{HC}(\text{NH}_2)_2\text{I}$  (Formamidinium iodide, FAI) was synthesized by dissolving formamidine acetate (Sigma-Aldrich) powder in a 1.5 molar excess of hydroiodic acid (HI; Sigma-Aldrich), 57 wt% in  $\text{H}_2\text{O}$ . After addition of acid, the solution was left stirring for 10 minutes at  $50^\circ\text{C}$ . Upon drying at  $100^\circ\text{C}$  for approximately 2h, a yellow-white powder was formed. This powder was then washed three times with diethyl ether to remove excess  $\text{I}_2$ . The powder was later dissolved in ethanol heated at  $80^\circ\text{C}$  to obtain a supersaturated solution. Once fully dissolved, the solution was then placed in a refrigerator for overnight recrystallization. The recrystallization process resulted in formation of white flake-like crystals. The FAI flakes were later washed with diethyl ether three times. Finally, the FAI flakes were dried overnight in a vacuum oven at  $50^\circ\text{C}$ .

### (2) Preparation of $\text{FA}_{0.83}\text{Cs}_{0.17}\text{Pb}(\text{I}_{0.9}\text{Br}_{0.1})_3$ perovskite precursor solution:

1.4 M perovskite precursor solution was prepared using a 4 : 1 (v : v) mixed solvent from anhydrous dimethylformamide (DMF) and dimethyl sulfoxide (DMSO) (Sigma-Aldrich) with desired composition using precursor salts: formamidinium iodide (FAI), cesium iodide (CsI; Alfa Aesar), lead iodide ( $\text{PbI}_2$ ; TCI), lead bromide ( $\text{PbBr}_2$ ; TCI). The solution was made in a nitrogen-filled glovebox and kept stirring overnight at room temperature.

### (3) $\text{CyPF}_6$ synthesis:

$\text{CyPF}_6$  was prepared according to previously reported methods.<sup>[S1]</sup> Equimolar amounts of 2-[2-[2-chloro-3-[2-(1,3-dihydro-3,3-dimethyl-1-ethyl-2H-benz[e]indol-2-ylidene) ethylidene]-1-cyclohexen-1-yl]-ethenyl]-3,3-dimethyl-1-ethyl-1H-benz[e]indolium iodide (CyI) and sodium hexafluorophosphate (Sigma Aldrich) were dissolved in 5:1 MeOH:DCM and stirred for 15 minutes at room temperature. The crude product was collected using vacuum filtration with methyl hydroxideto wash and re-dissolved in dichloromethane (DCM) to filter through a plug of silica gel with DCM eluent to filter out unreacted precursors. Product purity was

performed using a Waters Xevo G2-XS QToF mass spectrometer coupled to a Waters Acquity ultrahigh pressure liquid chromatography (LC) system in both positive and negative modes and found to be >95%.

(4) Preparation of organic dye-perovskite mixed solution:

2-[2-[2-chloro-3-[2-(1,3-dihydro-3,3-dimethyl-1-ethyl-2H-benz[e]indol-2-ylidene) ethylidene]-1-cyclohexen-1-yl]-ethenyl]-3,3-dimethyl-1-ethyl-1H-benz[e]indolium hexafluorophosphate (CyPF<sub>6</sub>) and 1-Butyl-2-(2-[3-[2-(1-butyl-1H-benzo[cd]indol-2-ylidene)-ethylidene]-2-diphenylamino-cyclopent-1-enyl]-vinyl)-benzo[cd] indolium tetrafluoroborate (Cy1BF<sub>4</sub>, FEW Chemicals) was dissolved in DMF with a concentration of 30 mg mL<sup>-1</sup>. The solution was made in air and sonicated for 30 min at room temperature. The obtained dye solution was directly mixed with 1.4 M perovskite precursor with various volume ratio, e.g., 1:1, 2:1, 3:1 and 4:1.

#### *Device fabrication*

(1) Hole transport layer:

The received PEDOT:PSS solution (Clevios P VP.A14083) was first diluted with methanol (1:2, v:v). The films were spin-coated in air on a pre-cleaned indium tin oxide (ITO) substrate at a spin-coating speed of 4000 rpm for 40s. The films were then annealing at 150 °C for 10 min.

(2) Dye-perovskite active layer:

The dye-perovskite precursor solutions were mixed with desired ratios right before disposition, and were deposited through a two-step spin coating program (10 s at 1000 rpm and 32 s at 6000 rpm) with dripping of chlorobenzene as anti-solvent during the second step, 8 s before the end. All the films were annealed at 100 °C for 2 min.

(3) Electron transport layer:

[6,6]-phenyl-C<sub>61</sub>-butyric acid methyl ester (PC<sub>61</sub>BM, SOLENNEBV) was dissolved in chlorobenzene to obtain 20 mg/mL solution in a glovebox. The PCBM solution was stirred at

50 °C overnight and filtered before use with 0.22 µm polytetrafluoroethylene (PTFE) filter to remove possibly present large particles. The PC<sub>61</sub>BM layer was spin-coated on top of perovskite films at a speed of 1500 rpm for 40 s.

(3) Electrode deposition:

80 nm silver electrodes were thermally evaporated under vacuum of  $\sim 5 \times 10^{-6}$  Torr, at a rate of  $\sim 0.1$  nm s<sup>-1</sup>. Note that the temperature of the vacuum chamber was controlled under 40 °C during the evaporation of metal electrodes, as a higher temperature will cause possible degradation of the perovskite films.

*Characterization:* All the thin film samples used for spectroscopy characterization were spin-coated on z-cut quartz substrates with similar spin-coating parameters as described above for device fabrication. UV-vis-NIR and short-wavelength infrared absorption spectra were collected using a Bruker Vertex 80v Fourier transform infrared (FTIR) spectrometer fitted with a reflection/transmission accessory. PL spectra were collected with an intensified charge coupled device (iCCD, PI-MAX4, Princeton Instruments), with each sample photoexcited by a 400 nm picosecond pulsed diode laser (PicoHarp, LDH-D-C-405M). Time-resolved photoluminescence was collected by means of time-correlated single photon counting (TCSPC, PicoHarp300). The obtained PL decay curves were fitted with a single exponential function. The crystallinity of the films was characterized by X-ray Diffraction (XRD). All XRD Spectra were obtained on a Rigaku SmartLab X-ray diffractometer with CuK $\alpha$ 1 (1.54060 Å) and a HyPix-3000 2D hybrid pixel array detector, and operated at 40 kV with a 2 $\theta$  scan range of 10~80°. The surface morphology of the perovskite films was imaged using a SEM (Hitachi S-4300) at an accelerating voltage of 4 kV. Film thicknesses were determined using a surface profilometer (Veeco Dektak 150).

The optical pump/THz probe measurements utilized the output of an amplified laser system (Spectra Physics – Tsunami, Empower, Spitfire), which had a center wavelength of 800 nm, repetition rate of 1 kHz, and pulse duration of 35 fs. THz radiation was generated using

optical rectification in a 450- $\mu\text{m}$  thick GaP(110) crystal and detected via free-space electro-optic sampling in a ZnTe chip with 0.2 mm ZnTe(110) on 3 mm ZnTe(100). The 400-nm pump beam was generated by focusing the 800-nm laser beam onto a beta-barium borate (BBO) crystal. To record time-dependent decay traces, the change in peak THz amplitude was measured as a function of pump-probe delay time. In conjunction with the THz measurements, in-situ PL spectra were collected using a UV-visible mini spectrometer (Ocean Optics, USB200+) fitted with an optical fiber, collimating lens, and 435-nm long-pass filter. All measurements were taken under vacuum using thin films deposited on z-cut quartz substrates.

*Device Performance Measurements:* The current–voltage curves were recorded with a sourcemeter (Keithley 2400). Photoresponsivity was evaluated via custom-build Fourier transform photocurrent spectroscopy based on the Bruker Vertex 80v Fourier transform spectrometer. The light intensity was calibrated with a Newport-calibrated reference silicon photodiode. Frequency response measurements were obtained using a set of LEDs (Thorlabs) with various wavelengths (405 nm, 528 nm, 630 nm, 780 nm, 851 nm, 1050 nm, 1200 nm, 1300 nm, 1400 nm, 1500 nm and 1600 nm), modulated using an Agilent 33500B arbitrary wave function generator. The photocurrent responses of the photodiodes were recorded using a digital storage oscilloscope (Agilent MSO7054A).

*Charge-carrier mobility calculation:*

The charge carrier mobility  $\mu$  is given by

$$\mu = \frac{\Delta S A_{\text{eff}}}{Ne} \quad , \quad (\text{S1})$$

where  $\Delta S$  is the sheet conductivity of the perovskite thin film,  $A_{\text{eff}}$  is the effective area of the overlap of optical pump and THz probe pulse,  $N$  is the number of photoexcited charge carriers, and  $e$  is the elementary charge.

Assuming that the film thickness is much smaller than the THz wavelength, the sheet photoconductivity  $\Delta S$  of a thin film between two media of refractive indices,  $n_A$  and  $n_B$ , can be expressed as<sup>[S2,S3]</sup>

$$\Delta S = -\varepsilon_0 c (n_A + n_B) \left( \frac{\Delta T}{T} \right), \quad (\text{S2})$$

where  $\Delta T/T$  is the experimentally determined change in transmitted THz electric field amplitude. In our experiment,  $n_A = 1$  for vacuum and  $n_B = 2.13$  for the z-cut quartz substrate. The number of photo-excited charge carriers  $N$  can be determined using the following equation:

$$N = \varphi \frac{E\lambda}{hc} (1 - R_{\text{pump}}) (1 - T_{\text{pump}}), \quad (\text{S3})$$

where  $E$  is the energy contained in an optical excitation pulse of wavelength  $\lambda$ ,  $R_{\text{pump}}$  is the reflectivity of the sample at normal incidence of the excitation beam,  $T_{\text{pump}}$  transmittance of the pump beam, and  $\varphi$  is the ratio of free charge carriers created per photons absorbed (the photon-to-charge branching ratio).

Substituting Equations S2 and S3 into Equation S1, the following equation is obtained:

$$\varphi\mu = -\varepsilon_0 c (n_A + n_B) \frac{A_{\text{eff}} hc}{Ee\lambda (1 - R_{\text{pump}}) (1 - T_{\text{pump}})} \left( \frac{\Delta T}{T} \right). \quad (\text{S4})$$

Because  $0 \leq \varphi \leq 1$ , the effective mobility  $\varphi\mu$  represents a lower limit, which becomes identical to the actual mobility for full photon to free carrier conversion. To allow accurate determination of  $\varphi\mu$ , we ensured that excitation conditions were in the linear regime. It should also be noted that the determined charge carrier mobility arises from the contributions of both electrons and holes and that these contributions cannot be separated.

*Fits to THz photoconductivity transients:*

The overall recombination dynamics can be described by the following equation:

$$\frac{dn}{dt} = -k_3 n^3 - k_2 n^2 - k_1 n, \quad (S5)$$

where  $n$  is the charge-carrier density,  $k_1$  is the monomolecular rate constant,  $k_2$  is the bimolecular rate constant, and  $k_3$  is the Auger rate constant.

As the experimentally observed quantity in optical pump-THz probe measurements,  $\Delta T/T = x(t)$ , is proportional to the photoconductivity, it is also proportional to the carrier density.

$$n(t) = \varphi C x(t) \quad (S6)$$

The photon-to-charge branching ratio  $\varphi$  indicates the fraction of absorbed photons which are converted to charge carriers. The proportionality factor  $C = n_0/x_0$  is the ratio of the absorbed photon density  $n_0$  to the initial THz response at time zero  $x(0)$ , where

$$\tilde{n}_0 = \frac{E \lambda \alpha(\lambda)}{hc A_{\text{eff}}} (1 - R_{\text{pump}}) \quad (S7)$$

The absorbed photon density is a function of the absorption coefficient  $\alpha$  and reflectance  $R_{\text{pump}}$  of the sample at the excitation wavelength  $\lambda$  and of the effective overlap  $A_{\text{eff}}$  of the optical pump beam and THz probe beam. At high excitation fluences,  $x(0)$  is no longer proportional to  $n_0$ . The value of  $C$  is therefore determined using a value of  $x(0)$  within the regime where  $x(0)$  is linearly proportional to the excitation fluence.

An expression for the time-dependent THz dynamics can be obtained by substituting Equation S6 into Equation S5:

$$\begin{aligned} \frac{dx}{dt} &= -C^2 \varphi^2 k_3 x^3 - C \varphi k_2 x^2 - k_1 x \\ &= -A_3 x^3 - A_2 x^2 - A_1 x \end{aligned} \quad (S8)$$

with  $A_i = C^{i-1} \varphi^{i-1} k_i$ . The coefficient  $A_1$  is determined from time-resolved PL measurements, ( $k_1=1.7 \times 10^5 \text{s}^{-1}$  for pristine perovskite and  $k_1=1.4 \times 10^8 \text{s}^{-1}$  for 1:1 CyPF<sub>6</sub>-perovskite thin films) and  $A_2$  is determined via a global fit to a fluence dependent set of THz transients. The

coefficient  $A_3$  was set to zero as the maximum charge-carrier density achievable experimentally was insufficiently high to obtain a reliable value. Similar to the mobility calculation, we can only determine the values  $\phi k_2$  from our fits. These equal the actual decay rate constants  $k_3$ ,  $k_2$  and  $k_1$  in case the material exhibits full photon-to-free-charge conversion and are lower limits when  $\phi < 1$ .

To account for the spatially varying charge density profile, the fit routine takes into account the exponential charge density profile created by the pump beam by dividing the sample into 30 equally thick slabs and computing the decay function for all of these individually.

## Supporting Figures

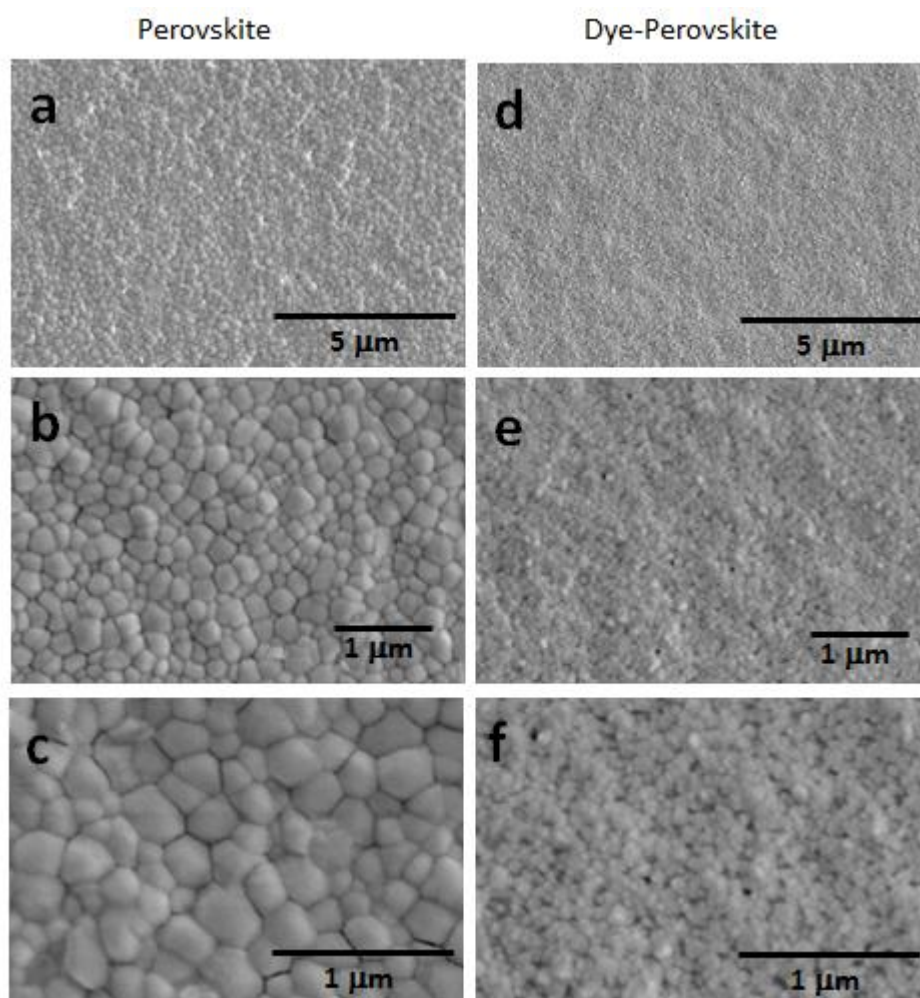


**Figure S1.** (a-c) Typical SEM images of the  $\text{FA}_{0.83}\text{Cs}_{0.17}\text{Pb}(\text{I}_{0.9}\text{Br}_{0.1})_3$  perovskite film and (d-f)  $\text{CyPF}_6$ -perovskite composite (2:1) film.

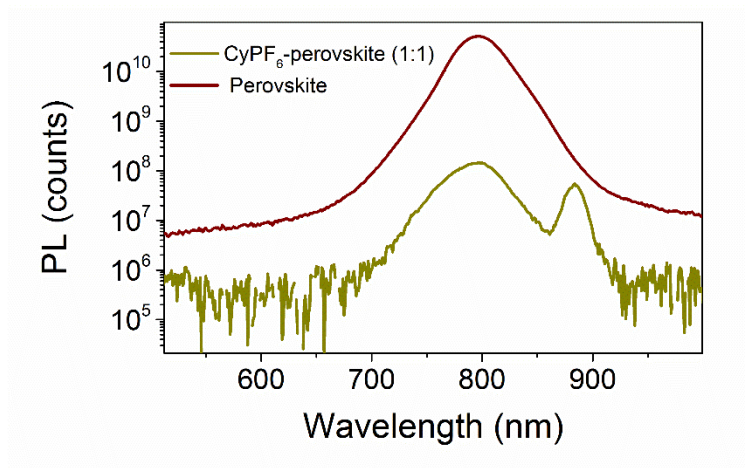


**Figure S2.** Comparison of the PL intensity of pristine perovskite and  $\text{CyPF}_6$ -perovskite composite (1:1) films. The composite films exhibit more than two orders of magnitude lower PL intensity compared to the pristine perovskite film, suggesting efficient PL quenching in the presence of  $\text{CyPF}_6$  molecules.

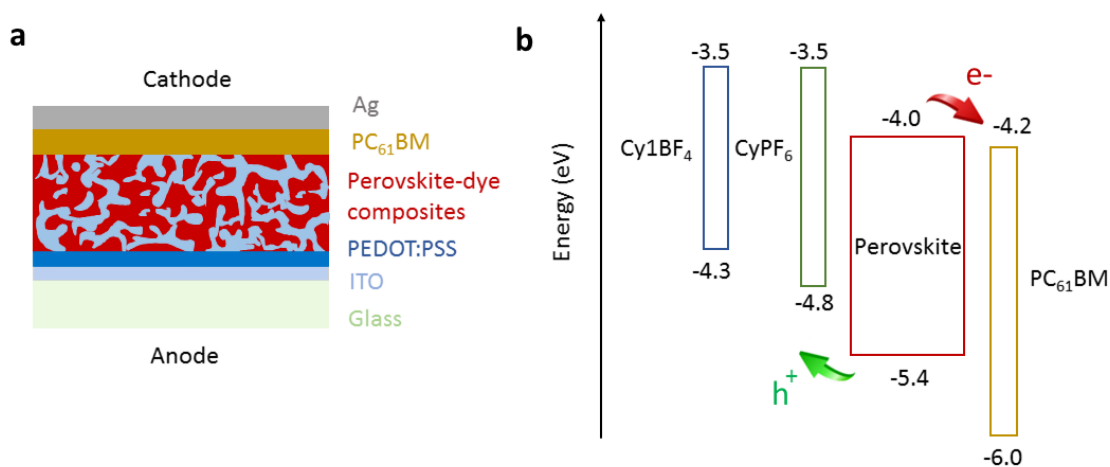


**Figure S3.** Schematic illustration of (a) device structure and (b) energy level diagram of perovskite, organic dyes ( $\text{CyBF}_4$  and  $\text{CyPF}_6$ ) and electron transport materials  $\text{PC}_{61}\text{BM}$ . Energy levels were retrieved from ref. 7, 44 and S4. Note: the valence band maximum and conduction band minimum of the perovskite indicating here are the value of  $\text{FAPbI}_3$ , which is the main component of the  $\text{FA}_{0.83}\text{Cs}_{0.17}\text{Pb}(\text{I}_{0.9}\text{Br}_{0.1})_3$  perovskite.

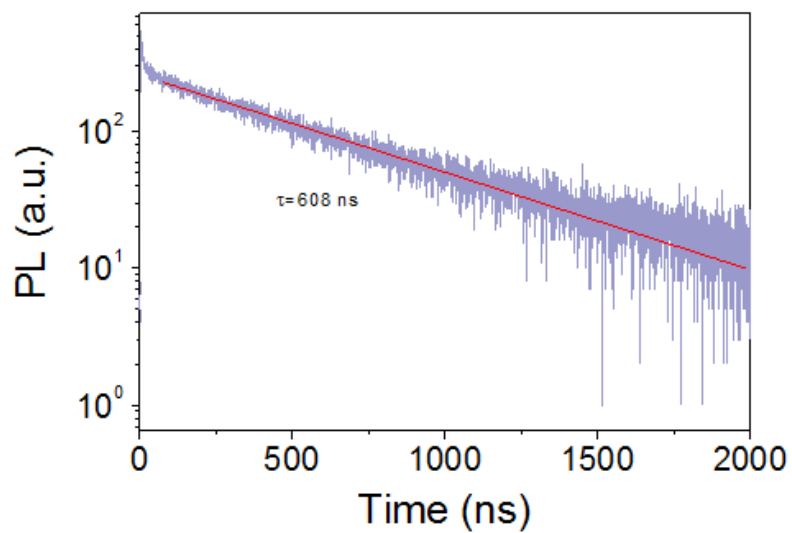


**Figure S4.** Typical time-resolved PL decay transient for a  $\text{FA}_{0.83}\text{Cs}_{0.17}\text{Pb}(\text{I}_{0.9}\text{Br}_{0.1})_3$  perovskite thin film. The film was excited at a wavelength of 532 nm; the PL was detected at a wavelength of 780 nm.

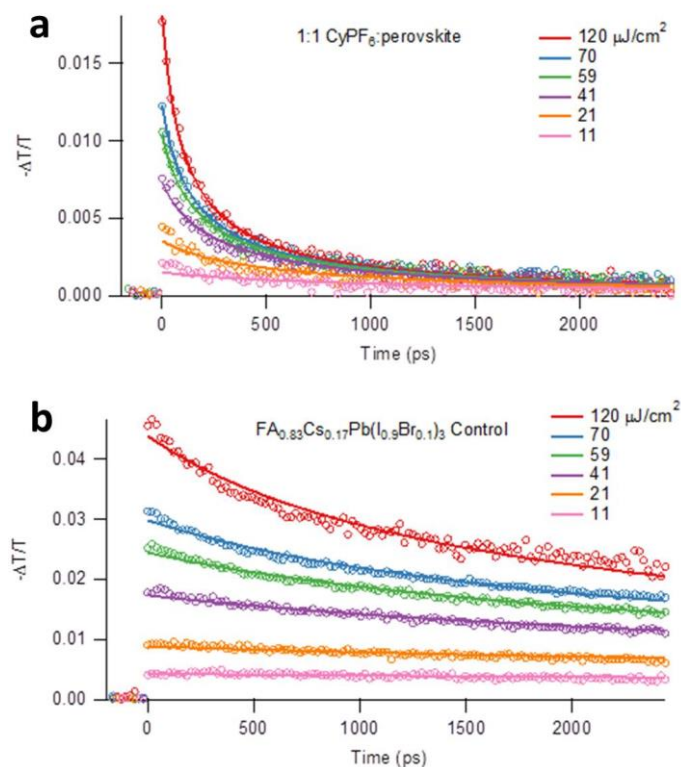


**Figure S5.** Optical pump/THz probe (OPTP) measurements of the charge-carrier dynamics in thin films of (a) CyPF<sub>6</sub>:perovskite (1:1) composite sample and (b) the FA<sub>0.83</sub>Cs<sub>0.17</sub>Pb(I<sub>0.9</sub>Br<sub>0.1</sub>)<sub>3</sub> control on z-cut quartz substrates. The open circles represent experimental data, and the solid lines are fits. The samples were excited at 400 nm with varying fluences as indicated on the graphs. Fits include the effective bimolecular recombination rate constant  $\phi k_2$  as a variable and the monomolecular recombination rate as constant input parameter determined from the PL transients ( $k_1=1.7\times 10^5\text{s}^{-1}$  for pristine perovskite and  $k_1=1.4\times 10^8\text{s}^{-1}$  for 1:1 CyPF<sub>6</sub>:perovskite thin films). Best fits (shown) yielded values of  $\phi k_2=5.3\times 10^{-11}\text{cm}^3\text{s}^{-1}$  for pristine perovskite and  $\phi k_2=1.7\times 10^{-9}\text{cm}^3\text{s}^{-1}$  for 1:1 CyPF<sub>6</sub>:perovskite thin films.

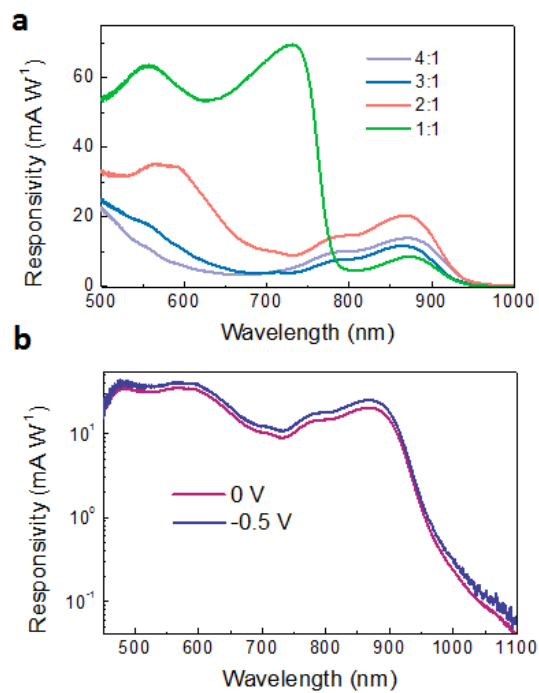


**Figure S6.** (a) Responsivity of the NIR photodiodes for active layers with various CyPF<sub>6</sub>-perovskite blend ratios and (b) typical electrical field dependent responsivity of the CyPF<sub>6</sub>-perovskite photodiodes.

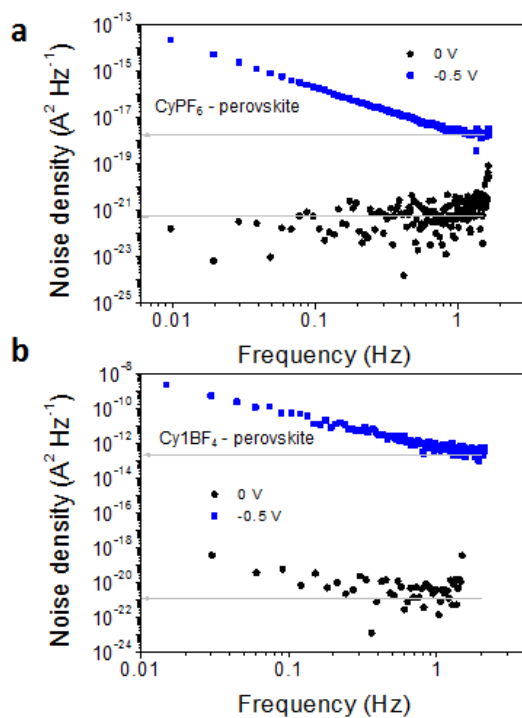


**Figure S7.** Typical noise density of (a) NIR photodiodes based on CyPF<sub>6</sub>-perovskite (2:1), and (b) SWIR photodiodes based on Cy1BF<sub>4</sub>-perovskite (2:1).

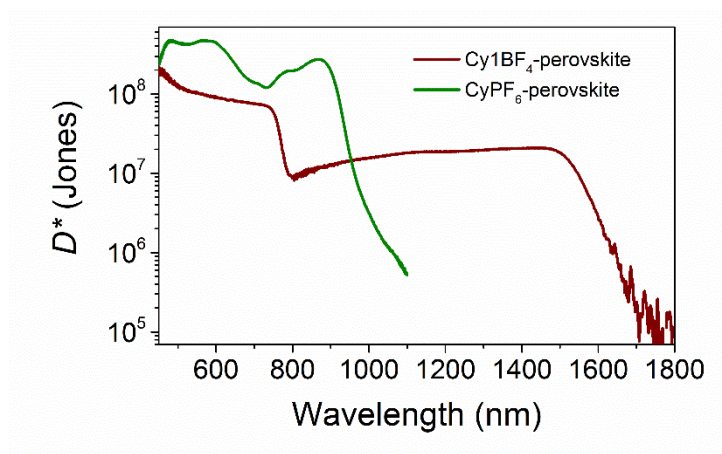


**Figure S8.** Typical specific detectivity of (a) NIR photodiodes based on CyPF<sub>6</sub>-perovskite (2:1), and (b) SWIR photodiodes based on Cy1BF<sub>4</sub>-perovskite (2:1) without bias.

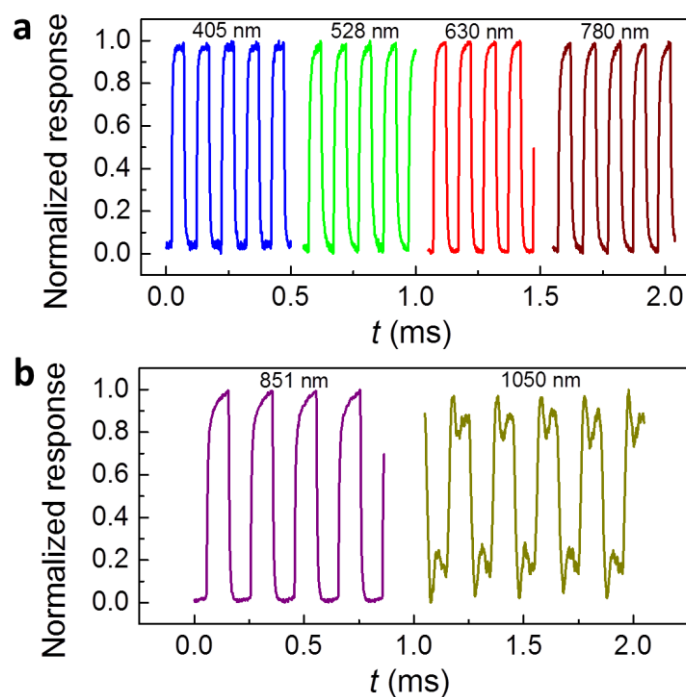


**Figure S9.** Temporal responses of the NIR photodiode based on CyPF<sub>6</sub>-perovskite to temporally modulated light sources with photon energies (a) above and (b) below the band gap of FA<sub>0.83</sub>CS<sub>0.17</sub>Pb(I<sub>0.9</sub>Br<sub>0.1</sub>)<sub>3</sub> perovskite.

Reference:

[S1]: J. Suddard-Bangsund, C. J. Traverse, M. Young, T. J. Patrick, Y. Zhao, R. R. Lunt, *Adv. Energy Mater.* **2016**, 6, 1501659.

[S2]: Nienhuys, H. K.; Sundström, V. *Phys. Rev. B*, **2005**, 71.

[S3]: Ulbricht, R.; Hendry, E.; Shan, J.; Heinz, T. F.; Bonn, M. *Rev. Mod. Phys.* **2011**, 83, 543.

[S4]: Kim H, Lim K G, Lee T W. *Energy Environ. Sci.*, **2016**, 9, 12.